FULL PAPER

Flexible Memory

ADVANCED
FUNCTIONAL
MATERIALS
www.afm-journal.de

Flexible Crossbar-Structured Phase Change Memory Array via Mo-Based Interfacial Physical Lift-Off

*Do Hyun Kim, Han Eol Lee, Byoung Kuk You, Sung Beom Cho, Rohan Mishra, Il-Suk Kang, and Keon Jae Lee**

Inorganic phase change memories (PCMs) have attracted substantial attention as a next-generation storage node, due to their high-level of performance, reliability, and scalability. To integrate the PCM on plastic substrates, the reset power should be minimized to avoid thermal degradation of polymers and adjacent cells. Additionally, flexible phase change random access memory remains unsolved due to the absence of the optimal transfer method and the selection device. Here, an Mo-based interfacial physical lift-off transfer method is introduced to realize a crossbar-structured flexible PCM array, which employs a Schottky diode (SD) selection device and conductive filament PCM storage node. A 32 × 32 parallel array of 1 SD-1 CFPCM, which utilizes a Ni filament as a nanoheater for low power phase transition, is physically exfoliated from the glass substrate at the face-centered cubic/body-centered cubic interface within the sacrificial Mo layer. First principles density functional theory calculations are utilized to understand the mechanism of the Mo-based exfoliation phenomena and the observed metastable Mo phase. The flexible 1 SD-1 CFPCM shows reliable operations (e.g., large resistance ratio of 17, excellent endurance over 100 cycles, and long retention over 10^4 s) with excellent flexibility. Furthermore, the random access operation is confirmed by addressing tests of characters "KAIST."

1. Introduction

With the advent of a future hyperconnected society, flexible electronics are being spotlighted as a core platform for the human–machine interface, based on their portability, shape adaptability, and human-friendly surfaces.[1–3] They offer a potentially wide number of unconventional form factors for electronics, ranging from soft consumer devices (e.g., rollable displays and wearable computers) to biointimate applications (e.g., skin-like smart sensors and implantable devices).[4–12] Flexible memories are considered to be an essential component for fully flexible electronic systems, because of their fundamental role in massive data processing, information storage, and inter-device communication.[13–15] Several researchers have studied flexible organic memories (e.g., charge-trap memory, ferroelectric memory, and resistive memory) utilizing spin-coating, ink-jet printing, and roll-based processes.[16–20] However, these memories have had inherent drawbacks, including insufficient performance, low durability, and difficult large-scale integration.[21,22]

Flexible inorganic memories are regarded as an attractive solution for advanced soft data-storage devices because they can provide excellent electrical properties, power efficiency, and reliability.[23–26] Nonetheless, there are significant challenges in realizing flexible inorganic memories, due to the intrinsic properties of plastic substrates and the lithographical limitations (e.g., high-temperature instability, multialignment inaccuracy, and complementary metal-oxide-semiconductor (CMOS) process incompatibility).[27–29] In recent years, several innovative approaches have been proposed to transfer high-temperature processed inorganic memories from conventional rigid substrates to polymers. For instance, inorganic-based laser lift-off, Ni stressor-based spalling, and direct wafer thinning methods have been reported,[30–32] however, complicated processing steps such as excimer laser process, electroplating, and wet chemical etching have resulted in low productivity and cost inefficiency. Therefore, a novel method eliminating these issues has to be developed to enable the highly effective transfer of ultrathin inorganic materials.

Inorganic phase-change memory (PCM), which utilizes reversible structural transition and corresponding resistance change of the phase change material,[33–35] has attracted a great deal of attention as a next-generation memory, considering its outstanding characteristics (e.g., fast switching speed, high reliability, and excellent nonvolatility) and scalability.[36–38]

D. H. Kim, Dr. H. E. Lee, Dr. B. K. You, Prof. K. J. Lee
Department of Materials Science and Engineering
Korea Advanced Institute of Science and Technology (KAIST)
291 Daehak-ro, Yuseong-gu, Daejeon 34141, Republic of Korea
E-mail: keonlee@kaist.ac.kr
Dr. S. B. Cho, Prof. R. Mishra
Department of Mechanical Engineering and Materials Science
and Institute of Materials Science and Engineering
Washington University in St. Louis
St. Louis, Missouri 63130, USA
Dr. S. B. Cho
Virtual Engineering Center
Technology Convergence Division
Korea Institute of Ceramic Engineering and Technology (KICET)
Jinju 52851, Republic of Korea
Dr. I.-S. Kang
National Nanofab Center
Korea Advanced Institute of Science and Technology (KAIST)
291 Daehak-ro, Yuseong-gu, Daejeon 34141, Republic of Korea

ADVANCED
SCIENCE NEWS
www.advancedsciencenews.com

ADVANCED
FUNCTIONAL
MATERIALS
www.afm-journal.de

One of the major obstacles in flexible PCM integration is the high operation power required during the reset process, since it causes thermal degradation of both adjacent cells and polymer substrates.[39–42] In our earlier work, we reported a highly power-efficient PCM operated by a self-structured conductive Ni filament nanoheater.[42] By controlling the filament diameter in nanoscale, the writing power could be significantly decreased to a reset current of 20 µA because the nanoheater shrank the switching volume of the phase-change material. Despite its remarkable potential as a nonvolatile storage node, the absence of an optimal selection device and the transfer method made it difficult to implement the crossbar-structured flexible phase-change random access memory (f-PRAM).

Herein, we report a Mo-based interfacial physical lift-off (IPLO) transfer method to realize flexible crossbar-structured PCM array employing one Schottky diode (SD, selection device) and one conductive filament PCM (CFPCM, storage node). A 32×32 parallel array of 1 SD-1 CFPCM for 1 kbit f-PRAM was fabricated on a Mo-based exfoliation layer, and subsequently transferred to a plastic substrate using the IPLO method. To understand the device exfoliation mechanism within competitive phases of the Mo layer, first-principles density-functional theory (DFT) calculations of enthalpies, phonon bands, and adhesive binding energies were performed under high uniaxial tensile strain. In addition, the energy barrier of the Mo phase transformation was computed to study the remaining Mo phase after the strain-induced exfoliation. The exfoliation phenomenon of the Mo-based IPLO was experimentally confirmed by X-ray diffraction (XRD) and transmission electron microscopy (TEM) analyses. Finally, the f-PRAM was successfully realized using the IPLO transfer method, showing the excellent flexibility of the ultrathin inorganic memory. Reliable flexible memory operations including set/reset switching, R_{HRS}/R_{LRS}, endurance, and retention were confirmed for stable data-storage on a plastic substrate. The random accessibility of the f-PRAM was also demonstrated by addressing tests under the worst-case scenario.

2. Results and Discussion

Figure 1a is a schematic illustration of the f-PRAM fabrication process using the IPLO transfer method. As an initial step, a Mo thin-film with body-centered cubic (BCC) phase was deposited on a rigid glass substrate as a sacrificial layer. A silicon dioxide (SiO_2) layer was uniformly deposited on the rapidly annealed Mo film as a mechanical buffer layer to prevent the inorganic memory from cracking and wrinkling during the IPLO process. After the heat treatment followed by the oxide deposition process, high uniaxial tensile strain was applied to the BCC Mo film, which induced a phase transformation from the BCC phase to the face-centered cubic (FCC) phase in the upper Mo layer. A crossbar-structured array of 1 SD-1 CFPCM was constructed on the SiO_2 buffer layer by integrating the CFPCM ($TiW/Ge_2Sb_2Te_5$, GST/NiO_x/Ni) on a current rectifying diode ($Pt/TiO_2/Ti$). The Ni filament nanoheater was formed within the NiO insulator by electrical stimulation, which enabled low-power switching of the phase change material (i.e., GST) by concentrating the current flow at the end of the nanofilament.

The Schottky contact of the Pt/TiO_2 interface was utilized as a selection device to minimize leakage current through the parallel interconnection. The integrated 1 SD-1 CFPCM memory array was physically exfoliated from the glass substrate at the FCC/BCC Mo interface, and was gently transferred to a polyethylene terephthalate (PET) film. Finally, the f-PRAM was successfully realized on a plastic substrate. (More details of the fabrication process are presented in the Experimental Section)

Figure 1b is the cross-sectional TEM image and the fast Fourier transform (FFT) pattern of the Mo thin-film deposited on a glass substrate. The pristine Mo presents a BCC crystal structure along the [111] zone axis. Figure 1c shows a high-resolution TEM (HRTEM) image and the corresponding FFT pattern of the exfoliated Mo on buffer SiO_2 after the IPLO process. The result shows that the exfoliated Mo had a FCC lattice along the [110] zone axis. These dissimilar Mo lattices of the pristine and exfoliated Mo indicate that the device exfoliation resulted from the BCC to FCC Mo phase transformation. Figure 1d presents a cross-sectional scanning electron microscopy (SEM) image of the memory stack before and after the IPLO process. The inorganic memory successfully retained its device structure without any mechanical degradation during the transfer step. Figure 1e is a photograph of the f-PRAM transferred onto a 12.5 µm thick PET substrate conformally attached to a rounded glass pipette of 7 mm diameter. As shown in the left inset, the memory exhibits excellent flexibility without any mechanical degradation such as cracks or wrinkles. The right inset in Figure 1e shows a magnified optical microscopy (OM) image of the stably transferred active cells and crossbar-structured interconnections of the 1 SD-1 CFPCM memory array.

To understand the mechanism of the IPLO phenomenon, in-depth investigations of the Mo-based exfoliation were conducted. As shown in the box-whisker plot of **Figure 2**a, the measured lattice constant value of the exfoliated Mo on the buffer oxide was 4.07 Å, which is larger than the theoretical FCC Mo a-axis lattice constant of 4.01 Å. Because the calculation using the generalized-gradient approximation (GGA) overestimates the lattice parameter than the experimental value, the larger lattice constant measured by XRD indicates that the exfoliated Mo was under residual tensile stress (see the Experimental Section).[43] As shown in Figure 2b, the residual stress of the exfoliated Mo was also evaluated with the XRD $\sin^2(\psi)$ technique[44] using the following equation

$$\sigma_f = \left(\frac{E}{1+\upsilon}\right)\cot\theta_0 \frac{\delta\theta}{\delta\sin^2\psi} \tag{1}$$

where σ_f is the residual stress of the Mo film, E is elastic modulus, υ is Poisson's ratio, θ is the Bragg angle of the stressed film, θ_0 is the Bragg angle of the unstressed film, $\delta\theta$ is the diffraction peak shift, and ψ is the angle between the normal directions of the plane and film. The residual stresses of the pristine and exfoliated Mo were calculated as 84.1 MPa and 1.752 GPa using the Equation (1), respectively. These results indicate that the tensile strain applied to the sacrificial Mo due to the heat treatment and buffer oxide deposition remained as a residual stress after the IPLO exfoliation. To investigate the strain-induced phase-transformation of the Mo, the energetics of the competing phases in the Mo thin-film were
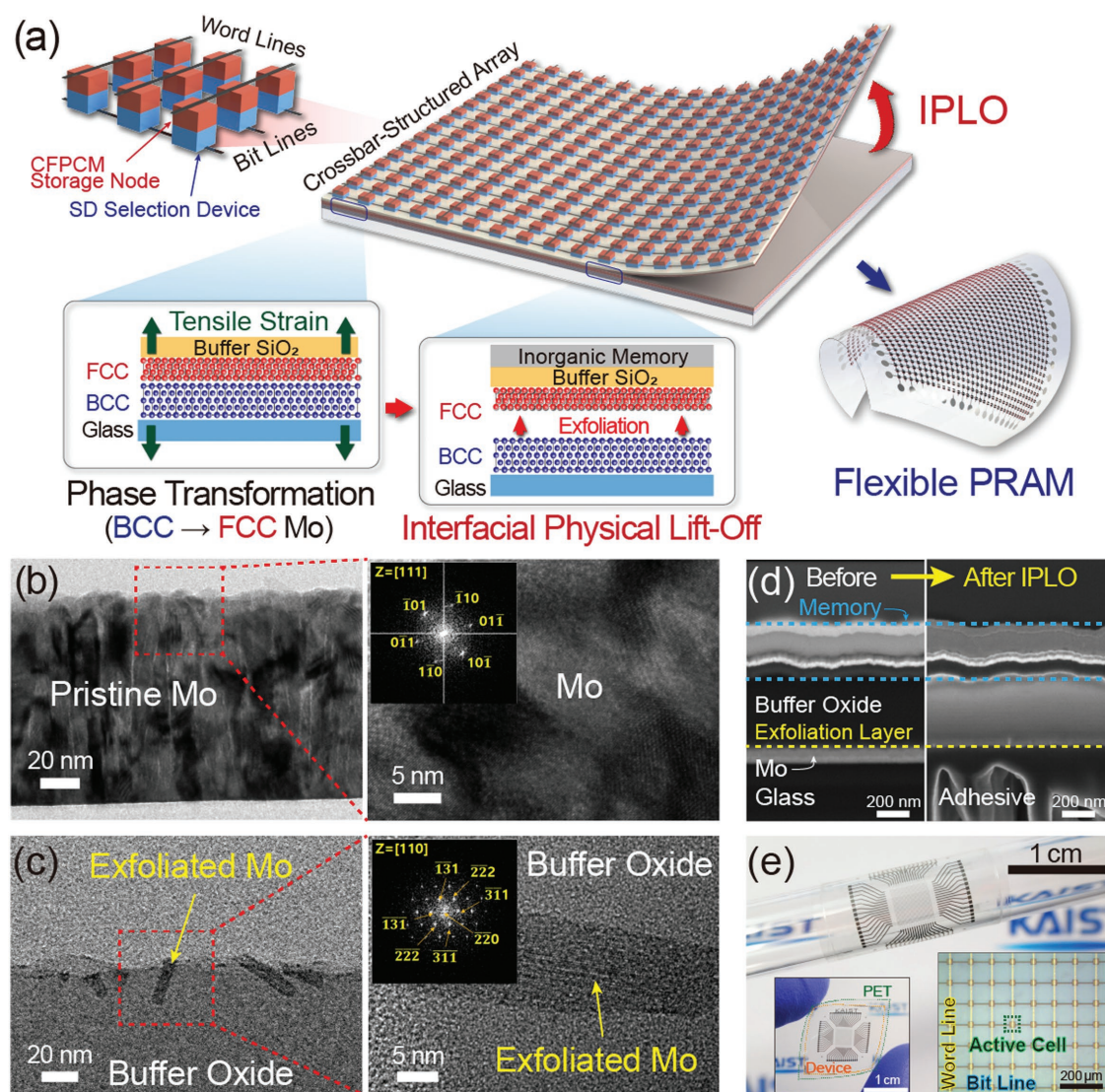
Figure 1. a) Schematic illustration of the f-PRAM fabrication using the IPLO process. b) Cross-sectional TEM image and the FFT result of the pristine Mo thin-film on rigid glass substrate. c) HRTEM image and the FFT result of the exfoliated Mo on buffer SiO_2. d) Cross-sectional SEM image of the Mo exfoliation layer, buffer SiO_2 layer, and memory stack before (left) and after (right) the IPLO process. e) Image of the f-PRAM conformally attached to a glass pipette with a diameter of 7 mm. The left inset shows the highly flexible f-PRAM realized on a 12.5 µm thick PET substrate. The right inset is the magnified OM image of the transferred f-PRAM active memory cells and interconnections.

studied using first-principles DFT calculations. Figure 2c shows the Mo crystal structure models of the [110]-stressed BCC and the [111]-stressed FCC Mo lattices utilized for DFT simulations, which are identical to the pristine and exfoliated Mo, respectively. The green arrows present the direction of the strain applied to the sacrificial Mo after heat treatment and buffer SiO_2 deposition. In Figure 2d, the enthalpies ($H = E + PV$) of the BCC and FCC Mo under uniaxial strain were calculated as a function of the interlayer distance d, where E is the calculated internal energy from DFT, P is pressure, and V is volume of the cell. The calculation result showed that the BCC Mo was more stable than the FCC phase under the strain-free condition. However, under the high uniaxial tensile strain of 2.77 Å $< d <$ 2.82 Å (colored in green), the FCC Mo became more stable than the BCC phase due to their enthalpy reversal,

as shown in the inset of Figure 2d. Figure 2e,f presents the calculated phonon band structures of the BCC and FCC Mo under high uniaxial tensile strain when the enthalpy reversal occurred. As shown in Figure 2e, the imaginary phonon modes of negative frequency indicate that the strained BCC phase Mo suffered dynamic instability.[45] In contrast, as shown in Figure 2f, the FCC phase Mo presented stable phonon band structure in the high-strain region. This dynamic instability of the BCC Mo compared to FCC Mo was the driving force that led to the BCC to FCC phase transformation.[45] Regarding the layer spalling of the IPLO exfoliation, the adhesive binding energy ($-W_{Adh}$) of the FCC/BCC interface, and the surface cleavage energies within BCC and FCC Mo were calculated as a function of interfacial distance d using DFT, as shown in Figure 2g and its inset. The universal binding-energy relation

**ADVANCED
SCIENCE NEWS**

www.advancedsciencenews.com

**ADVANCED
FUNCTIONAL
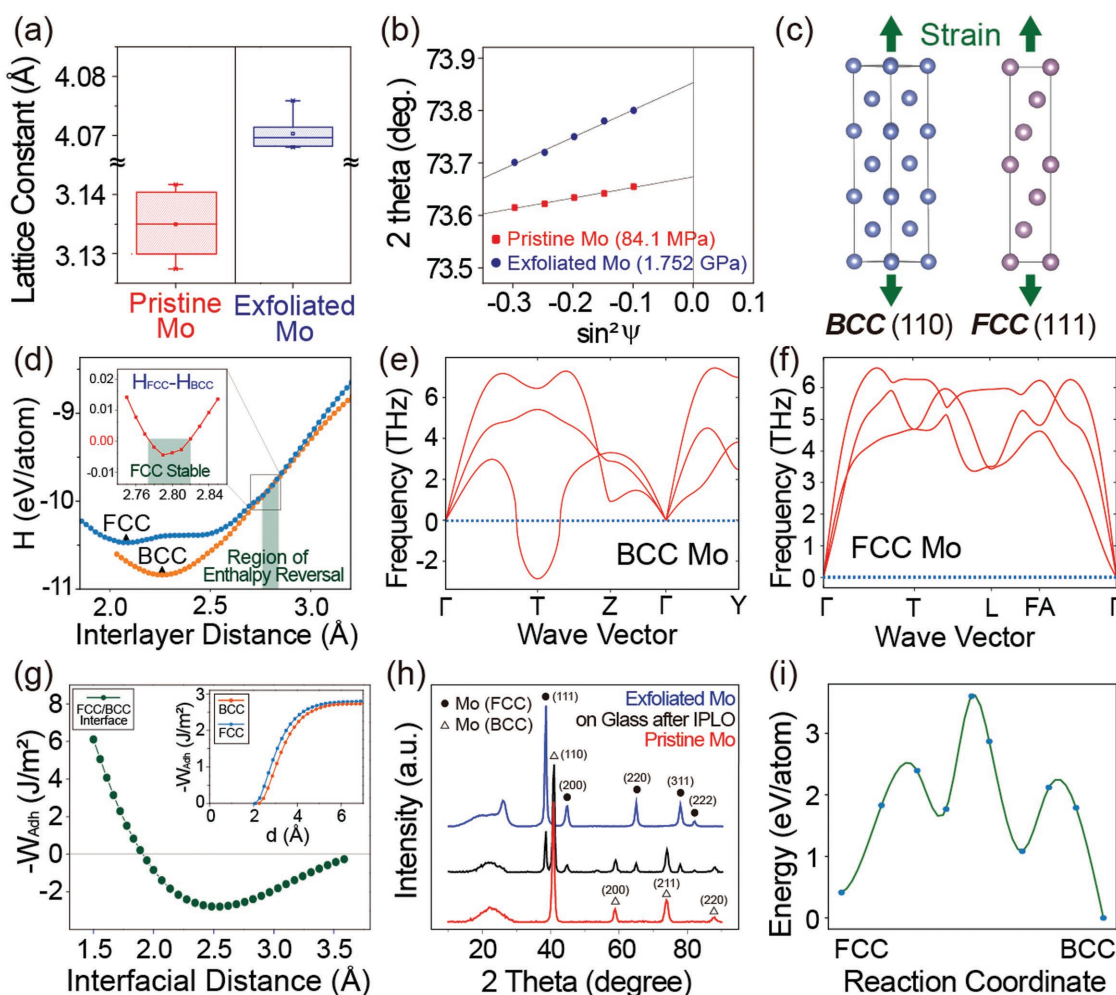MATERIALS**

www.afm-journal.de

Figure 2. a) A box-whisker plot showing the lattice constant distribution of the pristine Mo and exfoliated Mo. b) Residual stress analysis results of the pristine Mo and the exfoliated Mo using the XRD $\sin^2(\psi)$ technique. c) Illustration of the crystal structure of the [110]-stressed BCC and [111]-stressed FCC Mo lattices, with the applied uniaxial tensile strain shown in green arrows. d) The calculated enthalpies H of the BCC and FCC Mo as a function of interlayer distance d. e) Phonon band structure of the BCC Mo with uniaxial tensile strain along [110] ($d = 2.80$ Å). f) Phonon band structure of the FCC Mo under uniaxial tensile strain along [111] ($d = 2.80$ Å). g) The calculated adhesive binding energy of the FCC/BCC interface, BCC Mo and FCC Mo (inset) as a function of interfacial distance d. h) XRD analysis results of the pristine Mo on glass substrate (red), the remaining Mo on glass after IPLO exfoliation (black), and the exfoliated Mo (blue). i) Energy barrier curve of the FCC to BCC Mo phase transformation.

(UBER) was adopted as an analytic function to identify the energetics of cleavage.[46–48] The adhesion energy of the FCC/BCC interface was 1.56 J m^{-2}, which was lower than the FCC and BCC Mo surface cleavage energy of 2.44 and 2.37 J m^{-2}, respectively (see the Experimental Section). According to these theoretical results, the exfoliation of the Mo-based IPLO can be attributed to the combined effects of the strain-induced phase transformation followed by the FCC/BCC interface spalling.

Figure 2h presents the XRD results of the sacrificial Mo thin-film before and after the IPLO exfoliation process. XRD peaks of Mo remaining on the glass substrate mostly exhibit the BCC phase with a portion of the FCC phase, while the exfoliated Mo on the buffer oxide only shows the diffraction peaks of FCC Mo. This result is consistent with the DFT simulation, which indicated that the IPLO exfoliation occurred at the FCC/BCC interface. The slight portion of FCC Mo on the glass substrate can be explained by the nonuniform FCC/BCC interface

and the low surface formation energy of FCC Mo compared to BCC Mo under the high tensile strain of 2.19 Å < d < 2.92 Å (see Figure S2, Supporting Information). To interpret the FCC Mo on the buffer oxide after the strain-induced exfoliation, the energy barrier between the BCC and FCC Mo lattices was investigated using the DFT calculation. Figure 2i is the energy barrier curve of the FCC to BCC Mo phase transformation, simulated by the solid-state nudged elastic band method.[49] The FCC Mo is able to exist as a metastable phase without phase transition after the exfoliation, since a large energy barrier of 3.4 eV per atom exists between the FCC and the BCC Mo. Furthermore, the enthalpy curve in Figure 2d shows that the FCC Mo can exist in a metastable phase, since the flat basin region allows the FCC Mo to endure residual stress.

Figure 3 presents the device structure and the electrical performance of the f-PRAM. The reduction of the reset current was especially important in f-PRAM realization, since not
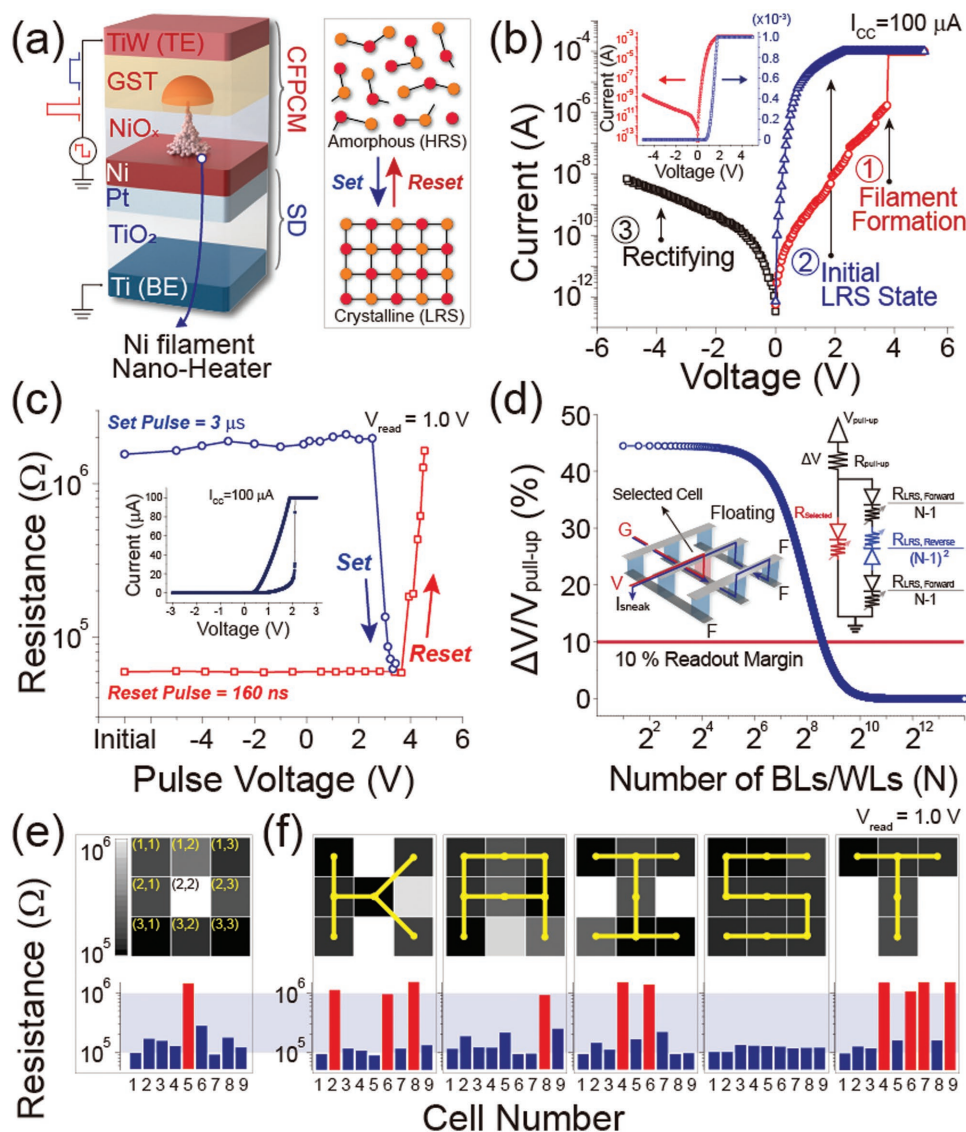
ADVANCED
SCIENCE NEWS
www.advancedsciencenews.com

ADVANCED
FUNCTIONAL
MATERIALS
www.afm-journal.de

Figure 3. a) Illustration presenting the device materials and structures of the f-PRAM unit cell (i.e., vertically stacked 1 SD-1 CFPCM cell). b) *I–V* characteristics of the integrated flexible 1 SD-1 CFPCM (i.e., f-PRAM unit cell) on a plastic substrate. The inset shows the rectifying *I–V* characteristics of the Schottky diode with a compliance current of 1 mA. c) Resistance–voltage pulse plot of the flexible 1 SD-1 CFPCM cell. The inset shows the *I–V* characteristics of the flexible 1 SD-1 CFPCM cell. d) Calculated readout margin as a function of the number of BLs and WLs. e) Histogram and corresponding color map presenting the resistance states of each memory cell within the 3 × 3 flexible 1 SD-1 CFPCM crossbar-array. f) Addressing test result of the 3 × 3 flexible 1 SD-1 CFPCM crossbar-array, spelling "KAIST."

only the current capacity of the diode was limited but also the large Joule heat could thermally degrade adjacent PCM cell, integrated Schottky diode, and polymer substrate.[37,50] It is reported in previous studies that the reset current of the PCM can be effectively reduced by increasing the heater resistance through shrinking the heater diameter.[50,51] The CFPCM in this study was able to reduce the reset current dramatically since the pointed cone-shaped Ni filament heater concentrated the current at the nanosized top vertex.[42] Without nanolithography patterning, the nanoscale Ni filament heater was formed beneath the GST through the migration of oxygen vacancies and Ni ions during initial electroforming step.[52] By applying operational pulses, the small portion of the chalcogenide

GST adjacent to the filament vertex switched its phase locally between amorphous and crystalline states,[42] which correspond to a high resistance state (HRS) and a low resistance state (LRS), respectively.[53] Each storage node was stacked directly on an SD selection device (Pt/TiO$_2$/Ti) to suppress the unintended leakage current flowing through the unselected neighboring cells. Minimizing the leakage current is important for f-PRAM implementation since it causes writing interference, reading disturbance, and undesirable power consumption in the crossbar-structured parallel architecture.[54–56] The vertically stacked 1 SD-1 CFPCM cell was integrated in the crossbar array with word lines (WLs) and bit lines (BLs) to achieve a 32 × 32 f-PRAM for 1 kbit data storage.

Figure 3b,c presents the operating characteristics of the vertically stacked flexible 1 SD-1 CFPCM cell utilized for f-PRAM implementation. As shown in the current–voltage (I–V) curve in Figure 3b, a positive voltage sweep was initially applied to form a Ni filament in the NiO insulating layer. The size of the filament could be tuned by controlling the compliance current (I_{cc}) during electroforming. In this work, I_{cc} of 100 µA was applied for optimum filament formation because low I_{cc} resulted in an easily breakable filament during PCM operation, while high I_{cc} resulted in a large PCM reset current. After the formation of the filament nanoheater, the flexible 1 SD-1 CFPCM cell was in the LRS with a cell resistance of 6.5×10^4 Ω at a read voltage (V_{read}) of +1 V. In negative voltage polarity, the memory showed a rectifying characteristic, due to the unidirectional conducting property of the integrated diode. The inset in Figure 3b presents the current rectifying characteristic of the single capacitor-like SD with a forward-to-reverse rectifying ratio of 5.17×10^6 at ± 1V(V_{read}). The voltage sweep was conducted with an I_{cc} of 1 mA to prevent permanent breakdown, which was sufficient to operate the flexible 1 SD-1 CFPCM cell (Figure S3, Supporting Information).

Figure 3c shows the resistance change of the f-PRAM unit cell during set and reset operations. Voltage pulses of 3 µs width and 160 ns width were applied for set (switching the GST to crystalline phase) and reset (switching the GST to amorphous phase) operations, respectively. As shown in the resistance–voltage pulse (R–V) plot, the flexible 1 SD-1 CFPCM cell successfully switched between LRS and HRS with a resistance ratio of 22.8 at a V_{read} of +1 V in the forward bias region. Statistical data of the operating voltages and the resistance distributions for 30 individual memory cells are presented in Figure S4 in the Supporting Information. The resistance of the LRS and HRS cells showed good uniformity with narrow distribution within one order, without an overlapping region at a V_{read} of +1 V. In addition, the HRS cell resistance of 1.88×10^6 Ω was 17 times higher than the LRS cell resistance of 1.11×10^5 Ω, indicating a large resistance ratio for practical operations.[57] During the negative voltage pulse, the flexible 1 SD-1 CFPCM cell exhibited no resistance switching between LRS and HRS. This unipolar switching behavior was attributed to the integrated rectifying SD selection device. In contrast, as shown in Figure S5 in the Supporting Information, the CFPCM without a selection device exhibited resistive switching in both voltage polarities. As shown in the inset in Figure 3c, the unipolar switching behavior was also demonstrated by the I–V characteristics of the memory. In addition, reliability of the flexible 1 SD-1 CFPCM cell was assessed, as shown in Figure S6 in the Supporting Information. During the endurance test, the flexible memory stably and consistently switched between HRS and LRS for more than 100 cycles. Furthermore, excellent data retainability was also demonstrated by 10^4 s duration of retention test. These results showed that our memory cell was suitable for implementing the crossbar-structured 32 × 32 f-PRAM.

To expand the flexible 1 SD-1 CFPCM cell into a high-density crossbar-structure, the maximum array size with at least 10% readout margin was calculated. Figure 3d presents the normalized readout margin ($\Delta V/V_{pull-up}$) of the expanded $N \times N$ 1 SD-1 CFPCM array, where N is the number of WLs and BLs. One bitline pull-up (OBPU) scheme was utilized as a readout method
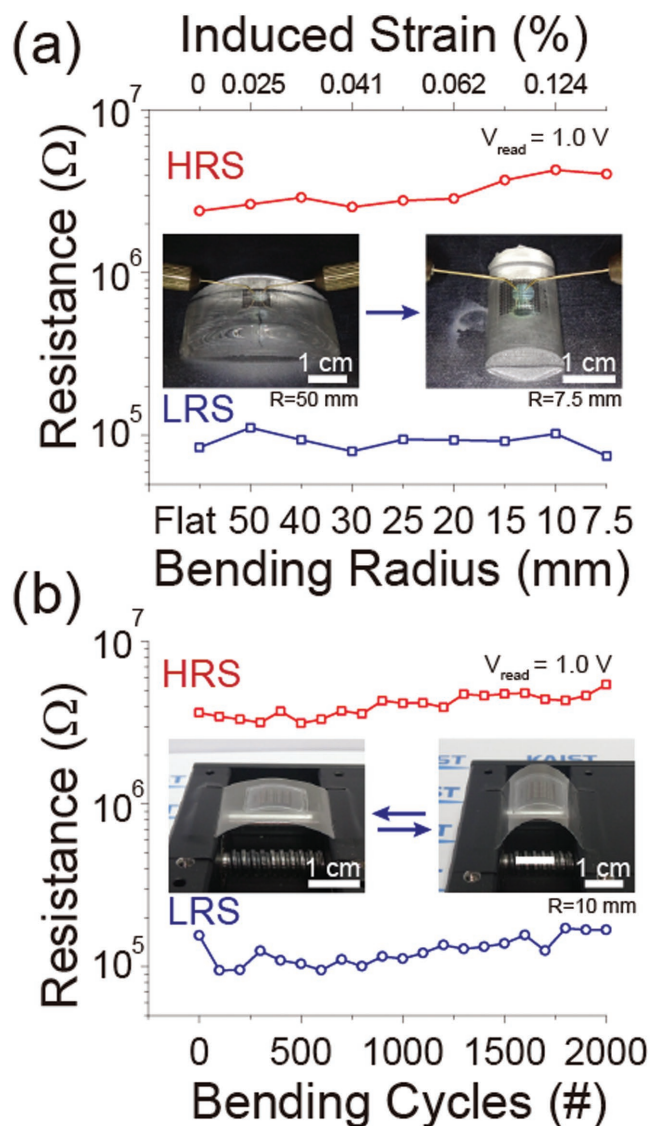

Figure 4. Mechanical reliability assessment results, tested by measuring the cell resistance of the f-PRAM unit cell as a function of bending radius and cycles. a) The measured cell resistance and calculated induced strain in the GST film while increasing the curvature from a flat state to a 7.5 mm bending radius. b) Measured cell resistance during repeated bending, up to 2000 cycles. The insets show the f-PRAM placed on the bending stage to evaluate flexibility.

with the assumption of worst-case scenario (i.e., all the unselected cells are in LRS),[58] as shown in the left inset in Figure 3d. The right inset is a simplified equivalent circuit of an $N \times N$ parallel crossbar array with leakage paths at read operation. The result indicated that the maximum allowed $N \times N$ array of the 1 SD-1 CFPCM could be scaled up to 380 × 380 for a tolerable 10% readout margin, with the adoption of an additional periphery circuit. (The detailed calculation is provided in the Supporting Information.) The maximum array size could be further increased by using a rectifying diode with large resistance in reverse bias or by tuning the CFPCM cell to present a large resistance ratio at V_{read}. In addition, we believe that the flexible crossbar-structured PCM array can be scaled down to maximize the bit density with

careful considerations on thermal design, selection device, and interconnection resistance.[37,50,59,60]

As shown in the resistance-based color map in **Figure 4**e, the random accessibility of the f-PRAM was demonstrated by operating the 3 × 3 crossbar-structured flexible 1 SD-1 CFPCM array in a worst-case scenario. A positive voltage sweep was initially applied to all the cells as a nanoheater forming step, which switched the memory cells to LRS. A reset voltage pulse was applied to switch the cell positioned in the center of the array from LRS to HRS. Using the OBPU readout scheme, a clear difference in the resistance of the (2, 2) memory cell was successfully sensed, showing that the integrated SD effectively suppressed the leakage current. As shown in Figure 4f, an additional readout test was conducted to confirm the addressing ability of the f-PRAM by programming and reading the characters "KAIST." These results clearly verified that the fabricated flexible 1 SD-1 CFPCM crossbar-array can operate without electrical interference by integrating rectifying diodes with each memory cell.

In order to evaluate the bending reliability of the f-PRAM, resistances of the LRS and HRS memory cells were measured at various bending conditions. As shown in Figure 4a, the f-PRAM unit cell stably retained its memorized state even when its curvature increased from a flat state to a 7.5 mm bending radius. As shown in Figure 4b, the f-PRAM unit cell exhibited a negligible change in resistance during 2000 repetitive bending cycles with a 10 mm bending radius. In both tests, the resistances of the LRS and HRS memory cells were clearly distinguished, with a resistance ratio over 20. The insets in Figure 4 show the f-PRAM mounted on the bending stage for the mechanical reliability evaluation. Additional bending test results including Y-axis direction bending and statistical data can be found in Figure S7 in the Supporting Information. To theoretically assess the mechanical robustness of the f-PRAM, the position of the neutral plane and the induced strain in the memory layer (i.e., GST) were calculated[61] (see the Supporting Information for the detailed calculations). The mechanical neutral plane was located 12.73 µm away from the bottom surface of the PET. The induced strain in the GST layer at 10 mm radius of curvature corresponds to 0.124%, which was less than the crack forming strain of 0.6%. These results explained the excellent flexibility of the inorganic-based f-PRAM, which was achieved using the optimized IPLO process. A comparison between the demonstrated f-PRAM with other reported flexible memories is presented in Tables S1 and S2 in the Supporting Information.

3. Conclusion

In conclusion, we demonstrated a crossbar-structured 32 × 32 f-PRAM using the Mo-based IPLO method. A crossbar 1 SD-1 CFPCM array on sacrificial wafers was successfully exfoliated at the FCC/BCC Mo interface on a glass substrate and subsequently transferred to a plastic substrate without degradation, to implement a flexible inorganic memory with 1 kbit data storage. Using the current concentration effect of the Ni filament nanoheater, the low power CFPCM was integrated with an oxide-based SD in a parallel array on a plastic substrate to minimize the electrical interference with adjacent cells. Residual stress analysis and first-principles DFT calculations

confirmed that the high uniaxial tensile strain was the reason for the BCC to FCC phase transformation observed in the upper Mo thin-film. The low adhesion energy of the FCC/BCC Mo interface compared to the surface cleavage energy within the BCC and FCC Mo enabled the IPLO exfoliation at the interface, as confirmed by TEM and XRD analysis. The flexible 1 SD-1 CFPCM demonstrated reliable memory operations with excellent bending stability on a plastic substrate, including a large resistance ratio over 17, excellent endurance over 100 cycles, and long retention over 10^4 s. The random accessibility of the f-PRAM was verified by addressing tests of operating 3 × 3 array of crossbar-structured 1 SD-1 CFPCM which performed without disturbance. We believe that the proposed IPLO strategy provides a highly effective method for achieving largely integrated flexible electronics such as flexible processors, displays, and memory devices.

4. Experimental Section

Fabrication of the IPLO Substrate: A rigid glass wafer (Corning glass, 700 µm in thickness) was initially prepared as a mother substrate. After ultrasonic cleaning the substrate with acetone, isopropyl alcohol, and deionized water, a molybdenum (Mo, 100 nm in thickness) thin-film was deposited on the substrate using a radio frequency (RF) sputtering process. Subsequently, the Mo thin-film was heat-treated in an oxygen (O_2) ambient environment (pressure of 10 Torr) at 600 °C for 1 min utilizing the rapid thermal annealing process. After cooling the substrate down to room temperature, a silicon dioxide (SiO_2, 500 nm in thickness) buffer layer was deposited using plasma-enhanced chemical-vapor deposition at 300 °C.

Fabrication of the 1 SD-1 CFPCM Array on IPLO Substrate: As the bottom electrode (BE) of the SD selection device, titanium (Ti, 50 nm in thickness) was deposited in a 5 µm width line pattern by RF sputtering. Thereafter, titanium dioxide (TiO_2, 50 nm in thickness) was deposited on the entire substrate by plasma-enhanced atomic layer deposition (PEALD) using titanium-tetraisopropoxide (TTIP) as a precursor and oxygen plasma as an oxidizer, at a substrate temperature of 100 °C and pressure of 3 Torr. The PEALD process cycle sequence was TTIP injection (3 s), Ar purge (8 s), oxygen plasma (RF 120 W, 8 s), and Ar purge (10 s). A relatively thick TiO_2 layer was deposited to prevent the degradation of the rectifying Schottky barrier (Pt/TiO_2) by BE Ti diffusion during the following oxygen (O_2) plasma treatment on the Nickel (Ni) surface. To form a low-resistance ohmic contact between the Ti BE and the TiO_2 layer, the substrate was baked on a hot plate at a temperature of 350 °C for 10 s. Platinum (Pt, 30 nm in thickness) and Ni (45 nm in thickness) were successively deposited in a square pattern (25 µm × 25 µm size) by RF sputtering process, as the top electrode (TE) of the SD and the BE of the CFPCM, respectively. The top thin layer of Ni was oxidized to nickel oxide (NiO_x, 16 nm in thickness) by oxygen plasma treatment using inductively coupled plasma-reactive ion etching process. Lastly, $Ge_2Sb_2Te_5$ (140 nm in thickness) and titanium–tungsten (TiW, 70 nm in thickness) layers were deposited in a 5 µm width line pattern by RF sputtering, as the phase switching chalcogenide layer and the TE of the CFPCM, respectively.

IPLO Transfer Process of the Fabricated 1 SD-1 CFPCM Array: The epoxy-based (SU 8, Microchem) passivation layer was spin coated (thickness of 1.4 µm) on the fabricated 1 SD-1 CFPCM array to prevent any mechanical degradation during the transfer step. Adhesive tape (Magic Tape, Scotch) was attached to the passivation layer as an intermediate carrier film, and subsequently, the ultrathin device layer was detached from the rigid glass substrate by gently raising one edge of the carrier film. The detached device was then adhered to the flexible PET substrate (12.5 µm in thickness) using UV curable adhesive (Norland optical adhesive 73 (NOA73), Norland Products). Finally, the carrier tape film was removed by acetone.

First-Principles Calculations: All the first-principles DFT calculations were performed using the projector augmented-wave method, as implemented in the Vienna ab initio software package. The exchange-correlation energy between the electrons was described with the Perdew and Wang generalized-gradient approximation functional. Brillouin zone integration was sampled using the Monkhorst–Pack scheme with a density of 0.01 Å^{-1}. Ionic relaxations were carried out until the maximal Feynman–Hellman forces were less than 0.001 eV Å^{-1}, while allowing cell to relax in all direction except along the strain direction. To calculate the pressure accurately, a cut-off energy of 700 eV was adopted for the plane-wave basis set expansion. Phonon calculations were performed with the Phonopy package with the harmonic approximation method.

The GGA was adopted to calculate the exchange-correlation energy term.[43] Using the approximation typically results in a theoretically calculated lattice constant that is slightly larger (1–2%) than the experimental value. The observation that the experimental lattice constant (4.07 Å) was larger than the theoretical lattice constant (4.01 Å) in this research implies that the exfoliated Mo was under tensile strain.

Interface Adhesion Energy Calculation: Work of adhesion per unit area W_{Adh} was calculated as a function of interfacial distance d using the following equation

$$W_{Adh} = \frac{(E_{FCC} + E_{BCC} - E_{int})}{A} \qquad (2)$$

where E_{FCC} and E_{BCC} are total energies of the FCC Mo and BCC Mo, respectively, E_{int} is the total energy of the whole system, and A is the interface area. The interface adhesion energy of the FCC/BCC Mo interface was calculated using the UBER[46–48] as an analytical fitting function

$$W(d) = -W_0(1 + d_s)\exp(-d_s) \qquad (3)$$

where W_0 is the fitted adhesion energy at the equilibrium distance d_0, $d_s = (d - d_0)/l$ is scaling length, and l is the characteristic length.

Electrical Characterizations: All electrical measurements were conducted using a Keithley 4200-SCS semiconductor parameter analyzer with a pulse measurement unit (Keithley 4225-PMU) and a remote amplifier/switch (Keithley 4225-RPM). During device operation, voltage was applied at the TE while the BE was kept grounded.

Supporting Information

Supporting Information is available from the Wiley Online Library or from the author.

Acknowledgements

Conflict of Interest

The authors declare no conflict of interest.

[1] D. H. Kim, R. Ghaffari, N. S. Lu, J. A. Rogers, *Annu. Rev. Biomed. Eng.* **2012**, *14*, 113.

[2] S. H. Lee, C. K. Jeong, G. T. Hwang, K. J. Lee, *Nano Energy* **2015**, *14*, 111.

[3] A. Nathan, A. Ahnood, M. T. Cole, S. Lee, Y. Suzuki, P. Hiralal, F. Bonaccorso, T. Hasan, L. Garcia-Gancedo, A. Dyadyusha, S. Haque, P. Andrew, S. Hofmann, J. Moultrie, D. P. Chu, A. J. Flewitt, A. C. Ferrari, M. J. Kelly, J. Robertson, G. A. J. Amaratunga, W. I. Milne, *Proc. IEEE* **2012**, *100*, 1486.

[4] W. Gao, S. Emaminejad, H. Y. Y. Nyein, S. Challa, K. V. Chen, A. Peck, H. M. Fahad, H. Ota, H. Shiraki, D. Kiriya, D. H. Lien, G. A. Brooks, R. W. Davis, A. Javey, *Nature* **2016**, *529*, 509.

[5] G. T. Hwang, D. Im, S. E. Lee, J. Lee, M. Koo, S. Y. Park, S. Kim, K. Yang, S. J. Kim, K. Lee, K. J. Lee, *ACS Nano* **2013**, *7*, 4545.

[6] D. H. Kim, N. S. Lu, R. Ma, Y. S. Kim, R. H. Kim, S. D. Wang, J. Wu, S. M. Won, H. Tao, A. Islam, K. J. Yu, T. I. Kim, R. Chowdhury, M. Ying, L. Z. Xu, M. Li, H. J. Chung, H. Keum, M. McCormick, P. Liu, Y. W. Zhang, F. G. Omenetto, Y. G. Huang, T. Coleman, J. A. Rogers, *Science* **2011**, *333*, 838.

[7] H. E. Lee, S. Kim, J. Ko, H. I. Yeom, C. W. Byun, S. H. Lee, D. J. Joe, T. H. Im, S. H. K. Park, K. J. Lee, *Adv. Funct. Mater.* **2016**, *26*, 6170.

[8] D. Y. Park, D. J. Joe, D. H. Kim, H. Park, J. H. Han, C. K. Jeong, H. Park, J. G. Park, B. Joung, K. J. Lee, *Adv. Mater.* **2017**, *29*, 1702308.

[9] J. A. Rogers, Z. Bao, K. Baldwin, A. Dodabalapur, B. Crone, V. R. Raju, V. Kuck, H. Katz, K. Amundson, J. Ewing, P. Drzaic, *Proc. Natl. Acad. Sci. USA* **2001**, *98*, 4835.

[10] G. Schwartz, B. C. K. Tee, J. G. Mei, A. L. Appleton, D. H. Kim, H. L. Wang, Z. N. Bao, *Nat. Commun.* **2013**, *4*, 1859.

[11] T. Sekitani, H. Nakajima, H. Maeda, T. Fukushima, T. Aida, K. Hata, T. Someya, *Nat. Mater.* **2009**, *8*, 494.

[12] L. Z. Xu, S. R. Gutbrod, A. P. Bonifas, Y. W. Su, M. S. Sulkin, N. S. Lu, H. J. Chung, K. I. Jang, Z. J. Liu, M. Ying, C. Lu, R. C. Webb, J. S. Kim, J. I. Laughner, H. Y. Cheng, Y. H. Liu, A. Ameen, J. W. Jeong, G. T. Kim, Y. G. Huang, I. R. Efimov, J. A. Rogers, *Nat. Commun.* **2014**, *5*, 3329.

[13] A. A. Bessonov, M. N. Kirikova, D. I. Petukhov, M. Allen, T. Ryhanen, M. J. A. Bailey, *Nat. Mater.* **2015**, *14*, 199.

[14] M. T. Ghoneim, M. M. Hussain, *Electronics* **2015**, *4*, 424.

[15] S. T. Han, Y. Zhou, V. A. L. Roy, *Adv. Mater.* **2013**, *25*, 5425.

[16] K. J. Baeg, D. Khim, J. Kim, B. D. Yang, M. Kang, S. W. Jung, I. K. You, D. Y. Kim, Y. Y. Noh, *Adv. Funct. Mater.* **2012**, *22*, 2915.

[17] S. K. Hwang, I. Bae, R. H. Kim, C. Park, *Adv. Mater.* **2012**, *24*, 5910.

[18] Y. Ji, D. F. Zeigler, D. S. Lee, H. Choi, A. K. Y. Jen, H. C. Ko, T. W. Kim, *Nat. Commun.* **2013**, *4*, 2707.

[19] R. H. Kim, H. J. Kim, I. Bae, S. K. Hwang, D. B. Velusamy, S. M. Cho, K. Takaishi, T. Muto, D. Hashizume, M. Uchiyama, P. Andre, F. Mathevet, B. Heinrich, T. Aoyama, D. E. Kim, H. Lee, J. C. Ribierre, C. Park, *Nat. Commun.* **2014**, *5*, 3583.

[20] T. Sekitani, T. Yokota, U. Zschieschang, H. Klauk, S. Bauer, K. Takeuchi, M. Takamiya, T. Sakurai, T. Someya, *Science* **2009**, *326*, 1516.

[21] B. Cho, S. Song, Y. Ji, T. W. Kim, T. Lee, *Adv. Funct. Mater.* **2011**, *21*, 2806.

[22] L. Zhou, J. Y. Mao, Y. Ren, S. T. Han, V. A. L. Roy, Y. Zhou, *Small* **2018**, *14*, 1703126.

[23] A. M. Hussain, M. M. Hussain, *Adv. Mater.* **2016**, *28*, 4219.

[24] S. Kim, H. Y. Jeong, S. K. Kim, S. Y. Choi, K. J. Lee, *Nano Lett.* **2011**, *11*, 5438.

[25] H. G. Yoo, S. Kim, K. J. Lee, *RSC Adv.* **2014**, *4*, 20017.

[26] B. K. You, J. M. Kim, D. J. Joe, K. Yang, Y. Shin, Y. S. Jung, K. J. Lee, *ACS Nano* **2016**, *10*, 9478.

[27] G. A. T. Sevilla, J. P. Rojas, H. M. Fahad, A. M. Hussain, R. Ghanem, C. E. Smith, M. M. Hussain, *Adv. Mater.* **2014**, *26*, 2794.

[28] Y. S. Ji, Y. Yang, S. K. Lee, G. D. Ruan, T. W. Kim, H. L. Fei, S. H. Lee, D. Y. Kim, J. Yoon, J. M. Tour, *ACS Nano* **2016**, *10*, 7598.

[29] C. Li, L. L. Han, H. Jiang, M. H. Jang, P. Lin, Q. Wu, M. Barnell, J. J. Yang, H. L. L. Xin, Q. F. Xia, *Nat. Commun.* **2017**, *8*, 15666.

[30] D. H. Kim, H. G. Yoo, S. M. Hong, B. Jang, D. Y. Park, D. J. Joe, J. H. Kim, K. J. Lee, *Adv. Mater.* **2016**, *28*, 8371.

[31] S. Kim, J. H. Son, S. H. Lee, B. K. You, K. I. Park, H. K. Lee, M. Byun, K. J. Lee, *Adv. Mater.* **2014**, *26*, 7480.

[32] D. Shahrjerdi, S. W. Bedell, *Nano Lett.* **2013**, *13*, 315.

[33] T. Cao, J. Bao, L. Mao, *Adv. Theory Simul.* **2018**, *1*, 1700027.

[34] T. Cao, Y. Li, L. Tian, H. Liang, K. R. Qin, *ACS Appl. Nano Mater.* **2018**, *1*, 759.

[35] T. Cao, L. Tian, H. Liang, K. R. Qin, *Microsyst. Nanoeng.* **2018**, *4*, 7.

[36] G. W. Burr, B. N. Kurdi, J. C. Scott, C. H. Lam, K. Gopalakrishnan, R. S. Shenoy, *IBM J. Res. Dev.* **2008**, *52*, 449.

[37] S. W. Fong, C. M. Neumann, H. S. P. Wong, *IEEE Trans. Electron Devices* **2017**, *64*, 4374.

[38] R. E. Simpson, P. Fons, A. V. Kolobov, T. Fukaya, M. Krbal, T. Yagi, J. Tominaga, *Nat. Nanotechnol.* **2011**, *6*, 501.

[39] K. Derbyshire, *Solid State Technol.* **2011**, *54*, 7.

[40] B. H. Mun, B. K. You, S. R. Yang, H. G. Yoo, J. M. Kim, W. I. Park, Y. Yin, M. Byun, Y. S. Jung, K. J. Lee, *ACS Nano* **2015**, *9*, 4120.

[41] W. I. Park, B. K. You, B. H. Mun, H. K. Seo, J. Y. Lee, S. Hosaka, Y. Yin, C. A. Ross, K. J. Lee, Y. S. Jung, *ACS Nano* **2013**, *7*, 2651.

[42] B. K. You, M. Byun, S. Kim, K. J. Lee, *ACS Nano* **2015**, *9*, 6587.

[43] J. M. Skelton, D. Tiana, S. C. Parker, A. Togo, I. Tanaka, A. Walsh, *J. Chem. Phys.* **2015**, *143*, 064710.

[44] I. C. Noyan, T. C. Huang, B. R. York, *Crit. Rev. Solid State Mater. Sci.* **1995**, *20*, 125.

[45] A. Togo, I. Tanaka, *Scr. Mater.* **2015**, *108*, 1.

[46] A. Banerjea, J. R. Smith, *Phys. Rev. B* **1988**, *37*, 6632.

[47] T. Hong, J. R. Smith, D. J. Srolovitz, J. G. Gay, R. Richter, *Phys. Rev. B* **1992**, *45*, 8775.

[48] M. Koberidze, M. J. Puska, R. M. Nieminen, *Phys. Rev. B* **2018**, *97*, 195406.

[49] D. Sheppard, P. H. Xiao, W. Chemelewski, D. D. Johnson, G. Henkelman, *J. Chem. Phys.* **2012**, *136*, 074103.

[50] H. S. P. Wong, S. Raoux, S. Kim, J. L. Liang, J. P. Reifenberg, B. Rajendran, M. Asheghi, K. E. Goodson, *Proc. IEEE* **2010**, *98*, 2201.

[51] F. Xiong, M. H. Bae, Y. Dai, A. D. Liao, A. Behnam, E. A. Carrion, S. Hong, D. Ielmini, E. Pop, *Nano Lett.* **2013**, *13*, 464.

[52] D. S. Jeong, R. Thomas, R. S. Katiyar, J. F. Scott, H. Kohlstedt, A. Petraru, C. S. Hwang, *Rep. Prog. Phys.* **2012**, *75*, 076502.

[53] S. H. Lee, Y. Jung, R. Agarwal, *Nat. Nanotechnol.* **2007**, *2*, 626.

[54] G. W. Burr, R. S. Shenoy, K. Virwani, P. Narayanan, A. Padilla, B. Kurdi, H. Hwang, *J. Vac. Sci. Technol., B: Nanotechnol. Microelectron.: Mater., Process., Meas., Phenom.* **2014**, *32*, 040802.

[55] G. H. Kim, J. H. Lee, Y. Ahn, W. Jeon, S. J. Song, J. Y. Seok, J. H. Yoon, K. J. Yoon, T. J. Park, C. S. Hwang, *Adv. Funct. Mater.* **2013**, *23*, 1440.

[56] K. J. Yoon, G. H. Kim, S. Yoo, W. Bae, J. H. Yoon, T. H. Park, D. E. Kwon, Y. J. Kwon, H. J. Kim, Y. M. Kim, C. S. Hwang, *Adv. Electron. Mater.* **2017**, *3*, 1700152.

[57] R. Waser, R. Dittmann, G. Staikov, K. Szot, *Adv. Mater.* **2009**, *21*, 2632.

[58] J. J. Huang, T. H. Hou, C. W. Hsu, Y. M. Tseng, W. H. Chang, W. Y. Jang, C. H. Lin, *Jpn. J. Appl. Phys.* **2012**, *51*, 04DD09.

[59] J. Y. Seok, S. J. Song, J. H. Yoon, K. J. Yoon, T. H. Park, D. E. Kwon, H. Lim, G. H. Kim, D. S. Jeong, C. S. Hwang, *Adv. Funct. Mater.* **2014**, *24*, 5316.

[60] H. G. Yoo, M. Byun, C. K. Jeong, K. J. Lee, *Adv. Mater.* **2015**, *27*, 3982.

[61] S. I. Park, A. P. Le, J. A. Wu, Y. G. Huang, X. L. Li, J. A. Rogers, *Adv. Mater.* **2010**, *22*, 3062.